

Supporting Information

Microfluidic Paper-based Analytical Soft Actuators (μ PAC)

Koki Yoshida^{1,3}, Masahiro Tanakinoue^{1,2}, Hiroaki Onoe⁴ and Michinao Hashimoto^{3,*}

¹ Research Center for Autonomous Systems Materialogy, Institute of Integrated Research, Institute of Science Tokyo, Japan

² Institute of Science Tokyo, Department of Computer Science; 4259 Nagatsuta-cho, Midori-ku, Yokohama, Kanagawa 226-8502, Japan

³ Singapore University of Technology and Design, Engineering Product Development; 8 Somapah Road Singapore 487372

⁴ Keio University, Mechanical Engineering; 3-14-1 Hiyoshi, Kohoku-ku, Yokohama, 223-8522, Japan

* Correspondence: hashimoto@sutd.edu.sg; Tel.: +65 6499 4867

Table of Contents

- S1. Role of the cellulose paper for bending motion
- S2. Chamber areas of the μ PAC with $t = 0.18$ mm, $L = 7.5$ mm, and $E = 169.4$ kPa
- S3. Chamber areas of the μ PAC with $t = 0.40$ mm, $L = 10$ mm, and $E = 169.4$ kPa
- S4. Characteristics of the μ PAC with Ecoflex 00-10
- S5. Bending angles of the μ PAC with five pneumatic chambers
- S6. μ PAC with multiple pneumatic chambers
- S7. Color change of pH sensor
- S8. Color change ratio (R_c) of pH-sensing μ PAC
- S9. Color-changing behavior of the paper-based colorimetric chemical sensor
- S10. Temperature sensor
- S11. Supporting movie legends
- S12. Reference of Supporting Information

S1. Role of the cellulose paper for bending motion

This work demonstrated a unique design for a soft actuator that could be fabricated by DIW printing. In our design, 3D-printed square microchambers were sandwiched between pre-fabricated silicone thin-film substrates with different stiffnesses: a silicone thin film and cellulose paper. We selected cellulose paper as a substrate for the soft actuator due to its desirable properties, such as being non-stretchable yet flexible, which acted as a strain-limiting layer. In contrast, the silicone elastomer was used for pneumatic chambers due to its stretchability and flexibility, enabling the bending motion (**Fig. S1a**). If 3D-printed square microchambers were sandwiched between two silicone thin-film substrates with the same stiffness, no bending motion would occur, as both sides of the silicone thin films would expand simultaneously (**Fig. S1b**).

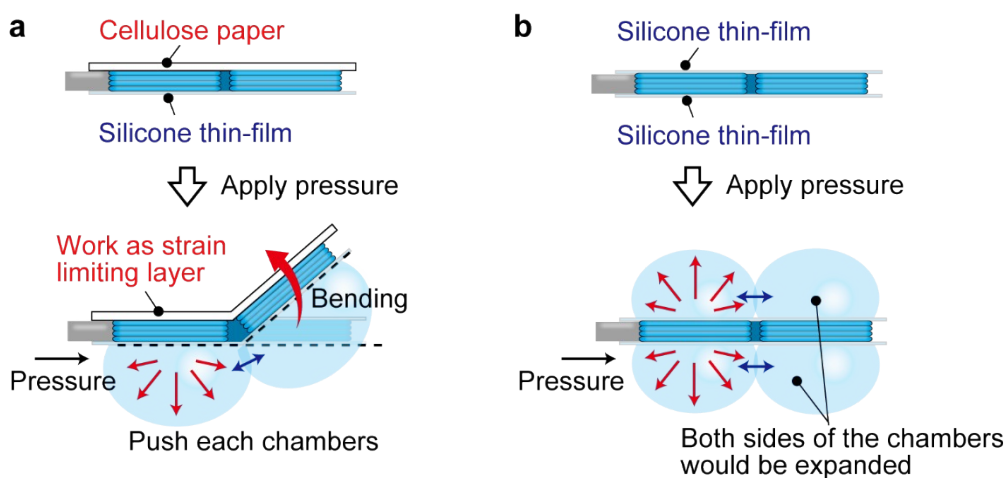


Figure S1. (a) Schematic illustration of bending motion of μ PAC. (b) Schematic illustration of the device with silicone thin films on both sides of the chamber.

S2. Chamber areas of the μ PAC with $t = 0.18$ mm, $L = 7.5$ mm, and $E = 169.4$ kPa

The cross-sectional areas of the back and front chambers (A_b and A_f , respectively) of μ PAC ($t = 0.18$ mm, $L = 7.5$ mm, and $E = 169.4$ kPa) were measured with varying pressure (p_a) (**Fig. S2**). At $p_a = 20$ kPa, $A_b = 139.8 \pm 27.9$ mm² and $A_f = 116.6 \pm 29.6$ mm² were measured. At 60 kPa, $A_b = 470.8 \pm 73.1$ mm² and $A_f = 338.7 \pm 33.7$ mm² were measured. The back chamber was more prone to expand than the front chamber. The same trend was observed with a different design of μ PAC with $t = 0.40$ mm, $L = 7.5$ mm, and $E = 169.4$ kPa.

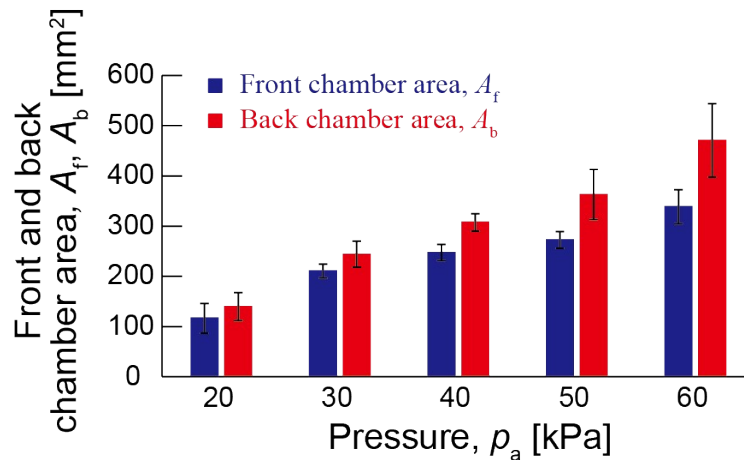


Figure S2. Plot showing the back and front chamber areas of μ PAC (A_b and A_f) with varying pressure (p_a). The parameter of μ PAC is $t = 0.18$ mm, $L = 7.5$ mm, and $E = 169.4$ kPa.

S3. Chamber areas of the μ PAC with $t = 0.40$ mm, $L = 10$ mm, and $E = 169.4$ kPa

The back and front chamber areas of μ PAC ($t = 0.40$ mm, $L = 10$ mm, and $E = 169.4$ kPa) were measured with varying pressure (p_a) (**Fig. S3**). Neither chamber expanded when $p_a < 60$ kPa. At $p_a = 60$ kPa, the back chamber started to expand ($A_b = 90.8 \pm 46.1$ mm²) while the front chamber remained relatively small ($A_f = 40.8 \pm 6.0$ mm²). In this condition, the chambers did not contact each other (**Fig. S3a top, Fig. S3b**). At $p_a = 110$ kPa, the front chamber was expanded, pushing each other ($A_f = 147.0 \pm 64.2$ mm², $A_b = 408.4 \pm 90.3$ mm², **Fig. S3a bottom**).

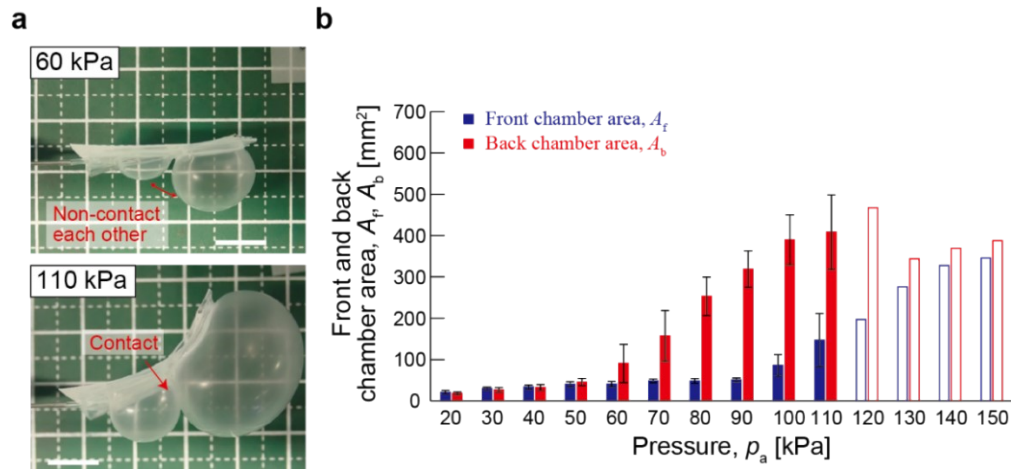


Figure S3. (a) Photographs showing the expansion of μ PAC with $t = 0.40$ mm, $L = 10$ mm, and $E = 169.4$ kPa at $p_a = 60$ kPa and 110 kPa. (b) Plot showing the back and front chamber areas of μ PAC with $t = 0.40$ mm, $L = 10$ mm, and $E = 169.4$ kPa with varying pressure (p_a). The unfilled bar in the plot suggests the measurements were done less than triplicate ($n = 3$). Scale bars: 10 mm.

S4. Characteristics of μ PAC with Ecoflex 00-10

Four types of μ PAC were fabricated with Ecoflex 00-10 ($E = 41$ kPa) at varying thickness ($t = 0.17$ mm, 0.41 mm) and chamber length ($L = 7.5$ mm, 10 mm). First, μ PAC ($L = 7.5$ mm, $t = 0.41$ mm) were characterized (**Fig. S4a**). The chambers did not expand significantly and the actuator did not show bending motion when $p_a < 70$ kPa ($\theta < 10^\circ$, **Fig. S4b blue triangles**). At $p_a = 140$ kPa, the maximum bending angle was obtained with $\theta = 72.2 \pm 10.4^\circ$. Next, μ PAC ($L = 7.5$ mm, $t = 0.17$ mm) were characterized. The bending angle ranged from $\theta = 8.1 \pm 2.8^\circ$ ($p_a = 20$ kPa) to $\theta = 70.3 \pm 3.8^\circ$ ($p_a = 120$ kPa) (**Fig. S4b orange diamonds**). The bending angle of this actuator was larger than the previous actuator ($L = 7.5$ mm and $t = 0.41$ mm). These results suggested that μ PAC with the thinner film (t) showed a larger degree of expansion and, thus a larger degree of bending (θ) when the same pressure was applied.

Then, we characterized the actuators with the increased chamber length ($L = 10$ mm). μ PAC ($L = 10$ mm, $t = 0.17$ mm) withheld up to $p_a = 180$ kPa, which was higher than the comparable device with $L = 7.5$ mm. The bending angle ranged from $\theta = 5.7 \pm 3.3^\circ$ ($p_a = 20$ kPa) to $\theta = 96.4 \pm 9.1^\circ$ ($p_a = 180$ kPa) (**Fig. S4b black squares**). Lastly, μ PAC ($L = 10$ mm, $t = 0.41$ mm) was shown to withhold the largest pneumatic pressure (230 kPa) among the devices that we investigated. The bending angle ranged from $\theta = 2.4 \pm 2.2^\circ$ ($p_a = 20$ kPa) to $\theta = 81.6 \pm 15.2^\circ$ ($p_a =$

180 kPa) (**Fig. S4b purple circles**). These experiments suggested that, when the same pressure was applied, the larger film thickness (t) resulted in a smaller bending angle of μ PAC (θ).

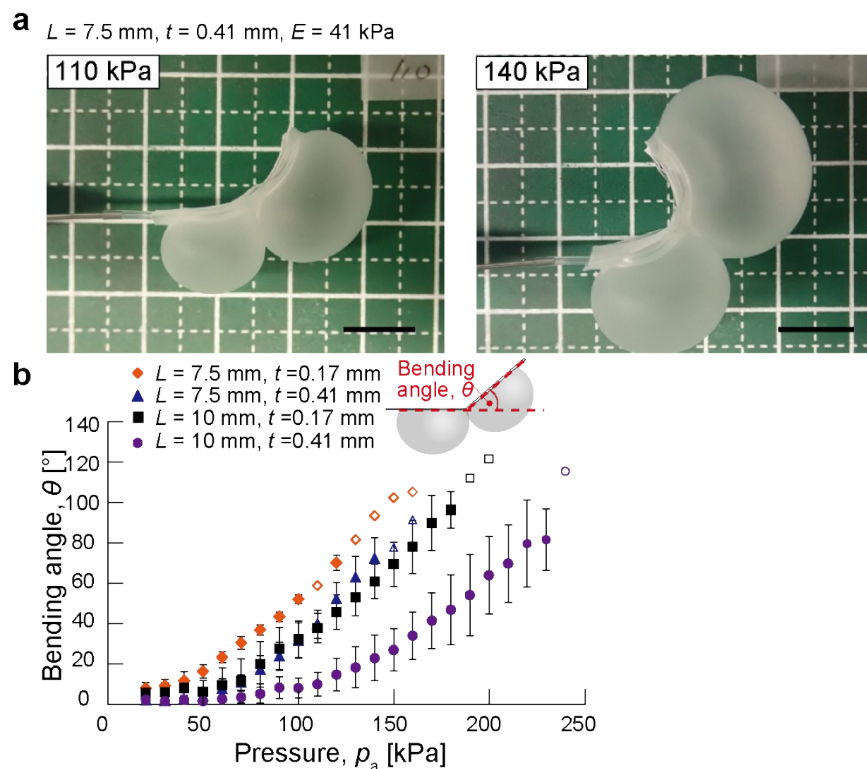


Figure S4. Characterization of μ PAC with Ecoflex 00-10. **(a)** Photographs showing the bending behavior of the μ PAC with EcoFlex 00-10. **(b)** Bending angle of μ PAC (θ) consisting of the film of Ecoflex 00-10. Unfilled marks indicate that the experiments were less than triplicate ($n = 3$).

Scale bars: 10 mm.

S5. Bending angles of μ PAC with five pneumatic chambers

The bending angles of μ PAC (θ_n , $n = 1, 2, 3, 4$) with five pneumatic chambers were studied (**Fig. S5a**). The bending angles were $\theta_1 = 36.6^\circ$, $\theta_2 = 48.5^\circ$, $\theta_3 = 42.6^\circ$, and $\theta_4 = 33.7^\circ$ as defined (**Fig. S5a, 5b**). θ_2 and θ_3 were relatively larger θ_1 and θ_4 . In the design of this actuator, the three chambers in the middle have two flow channels on each side. This arrangement may explain the ease of bending for the two joints in the middle and the larger bending angles for θ_2 and θ_3 than for θ_1 and θ_4 . Additional experiments would be necessary to verify this hypothesis.

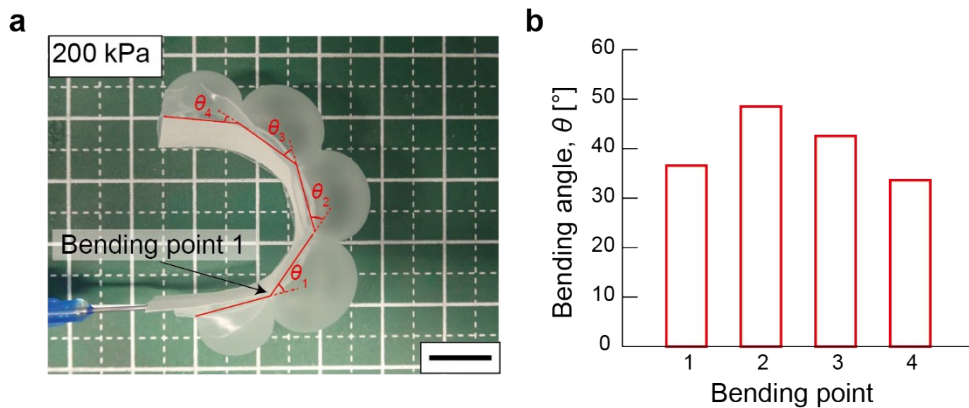


Figure S5. (a) Photograph showing the bending actuation of μ PAC with five pneumatic chambers. The bending angles (θ_n) are indicated in the photograph. **(b)** Plot showing the bending angle at each joint of the actuator. Scale bar: 10 mm.

S6. μ PAC with multiple pneumatic chambers

We designed two types of μ PAC with multiple pneumatic chambers. First, μ PAC with three pneumatic chambers ($L = 10$ mm) was actuated At $p_a = 250$ kPa, each bending angle was nearly 90° . At $p_a = 400$ kPa, each bending angle was nearly 120° , closing the loop of the actuator (Fig. S6a, b). A two-directional pneumatic chamber (e.g., cross-shape) was also fabricated (Fig. S6c). This two-directional μ PAC actuated and created a grasping motion.

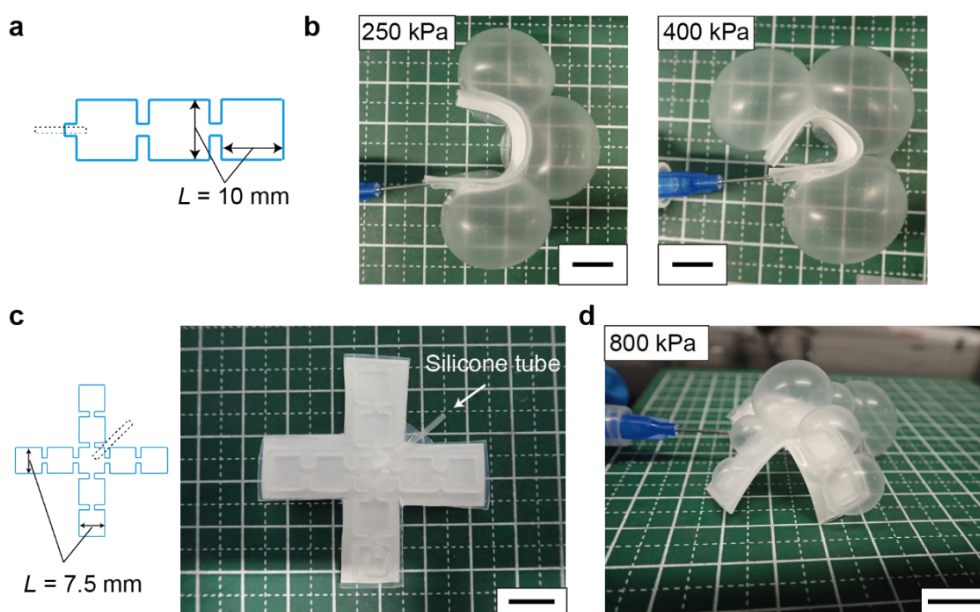


Figure S6. (a) Illustration of μ PAC with three pneumatic chambers. (b) Photographs showing the bending actuation of μ PAC at $p_a = 250$ kPa and $p_a = 400$ kPa. (c) Illustration and photograph of μ PAC with a crossing arrangement of nine chambers. (d) Photographs showing the grasping motion of the two-dimensional μ PAC. Scale bar: 10 mm.

S7. Color change of pH-sensing μ PAC

We observed the color change of the pH indicator using known pH solutions. We used phthalate pH standard solution (pH = 4, HORIBA Advanced Techno, Co., Ltd., Kyoto, Japan), phosphate pH standard equimolal solution (pH = 7, HORIBA Advanced Techno, Co., Ltd., Kyoto, Japan), tris hydrochloride acid buffer (pH = 8), and tetraborate pH standard solution (pH = 9, HORIBA Advanced Techno, Co., Ltd., Kyoto, Japan) to achieve known pH. The circular hydrophobic barrier was fabricated by patterning wax. Then, the pH indicator was enclosed inside the circular hydrophobic barrier to create the colorimetric pH sensor. The hue values of the pH indicator at different pH values were analyzed by ImageJ and compared with the previous study^[1]. The original color of the pH indicator, which was green, was initially analyzed (hue = 52.7) (**Fig. S7**). When applying the acidic solution (pH = 4), the color shifted to red (hue = 16.3). Conversely, the color shifted to blue by applying the alkaline solution. These results showed that the colorimetric pH sensor could detect whether the target samples were acidic or alkaline. In addition, the hue values of the pH indicator with pH = 7, 8, and 9 were measured as 53.9, 136.8, and 83.0, respectively. This observation suggested that the approximate pH can be estimated using the color of the pH indicator. However, because the pH values and the hue values of the indicator do not establish a simple linear relationship, additional data points are required to perform a reliable estimation of pH from the hue value.

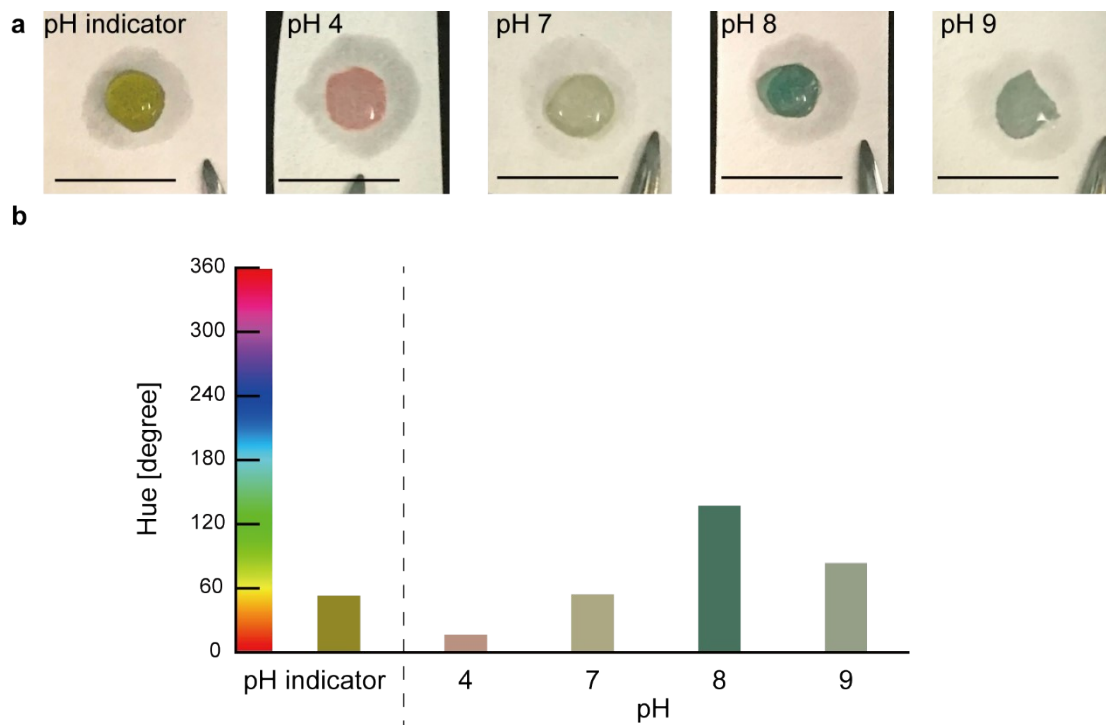


Figure S7. (a) Optical images showing the colors of the pH indicators enclosed in the wax well.

Scale bars are 10 mm. (b) The values of the hue of the pH indicators on the paper.

S8. Color change ratio (R_c) of pH-sensing μ PAC

We measured the color change ratios (R_c) when sensing Sample 1 (undamaged), Sample 2 (entirely damaged), and Sample 3 (partially damaged). The color change ratios of Sample 1 for Regions A and B were $R_c = 1.01$ and 1.02 , respectively (**Fig. S8a yellow bars**), suggesting that the color change was not apparent. In contrast, the color change ratios of Sample 2 for Regions A and B were $R_c = 1.07$ and 1.13 , respectively (**Fig. S8a pink bars**), suggesting the feasibility of detecting surface damage by the color change due to pH. Finally, the color change ratio of Sample 3 suggested the distinct contrast between Regions A and B, with $R_c = 1.02$ for Region A (undamaged) and $R_c = 1.22$ for Region B (damaged) (**Fig. S8b**).

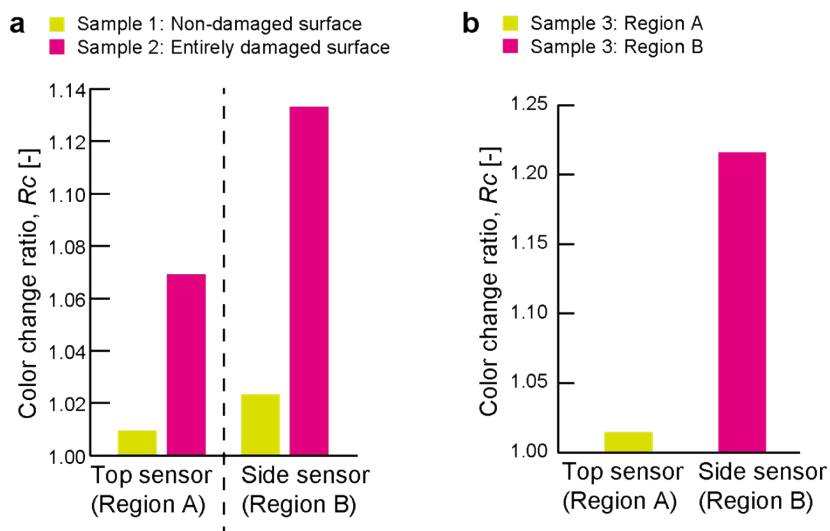


Figure S8. (a) The color change ratios (R_c) for Samples 1 and 2. **(b)** The color change ratio (R_c) for Sample 3.

S9. Color-changing behavior of the paper-based colorimetric chemical sensor

We observed the progress of the color change of the pH-sensing μ PAC over time. **Fig. S9** displays the time-resolved images of the colorimetric regions of μ PAC. Before contacting the surface, the reagent exhibited its original color (green). Upon contact with the damaged part of the lime, the pH indicator changed color to red within 1.5 s. Experimentally, we observed that the response of the pH-sensing μ PAC was only limited by the diffusion of the acidic juice from the lime to the sensing region of the paper. The color change occurred immediately after absorbing the aqueous sample. It is worth noting that the absorption of the aqueous sample did not compromise the bending motion of μ PAC in this experiment. This result suggests that μ PAC maintained contact with the curved surface of the lime while the pneumatic pressure was applied. The stability of the shape of the paper substrate upon wetting may depend on the chemical nature and absorbed volume of the target sample, which should be tailored to specific applications.

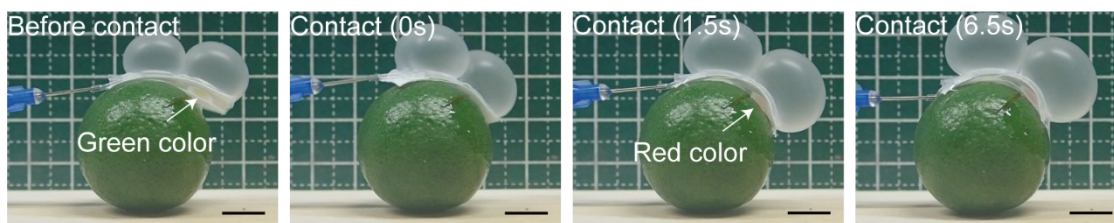


Figure S9. The color change and shape integrity of μ PAC during the actuation and the absorption of the wet sample. The reaction time is indicated in each time-resolved image. Scale bars are 10 mm.

S10. Colorimetric temperature sensor

To show the versatility of the platform, we demonstrated colorimetric temperature sensing using thermochromic ink embedded in the wax confinement. Thermochromic ink (P70-2637, NaRiKa Corporation, Tokyo, Japan) was used as a reagent. The temperature change (from room temperature, 25°C, to an elevated temperature, 40°C) facilitated the color change of the thermochromic ink from blue (hue = 214.5) to pink (hue = 344.5) (**Fig. S10**). This result suggested that different types of colorimetric sensing can be performed using μ PAC enclosing different functional inks.

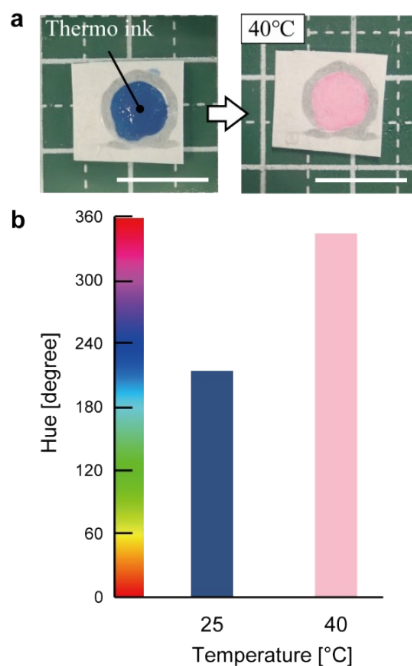


Figure S10. (a) Images illustrating the color change of the colorimetric temperature sensors. Scale bars are 10 mm. (b) Hue values of the colorimetric temperature sensors.

S11. Supporting movie legends

Supporting movie S1: Repeated actuation of the μ PAC

Supporting movie S2: Local detection of the partially damaged sample

S12. Reference of Supporting Information

[1] K. Yoshida, H. Onoe, *Adv. Intel. Syst.*, **2022**, 4, 5, 2100248, 1-9.